Research article

Renyuan Ren, Zile Li, Liangui Deng, Xin Shan, Qi Dai, Zhiqiang Guan, Guoxing Zheng* and Shaohua Yu

Non-orthogonal polarization multiplexed metasurfaces for tri-channel polychromatic image displays and information encryption

https://doi.org/10.1515/nanoph-2021-0259
Received May 24, 2021; accepted July 19, 2021;
published online August 2, 2021

Abstract: Interference usually occurs between two non-orthogonally polarized light beams. Hence, metasurface enabled polarization multiplexing is generally conducted under two orthogonal polarization states to realize independent intensity and/or phase modulations. Herein, we show that polarization multiplexed metasurfaces can work under three non-orthogonal polarization states to realize tri-channel image displays with independent information encoding. Specifically, enabled by orientation degeneracy, each nanostructure of the metasurface operates with triple-manipulations of light, i.e., two channels for independent intensity manipulation under $\pi/4$ and $3\pi/8$ linearly polarized (LP) light, respectively, and one channel for phase manipulation without polarization control. We experimentally demonstrate this concept by recording one continuous-brightness polychromatic image and one binary-brightness polychromatic image right at the metasurface plane, while a continuous-brightness polychromatic image is reconstructed in the far field, corresponding to three independent channels, respectively. More interestingly, in another design strategy with separated image encoding of two wavelengths, up to six independent image-display channels can be established and information delivery becomes safer by utilizing encryption algorithms. With the features of high information capacity and high security, the proposed metadevices can empower advanced research and applicati ons in multi-channel image displays, orbital angular momentum multiplexing communication, information encryption, anti-counterfeiting, multifunctional integrated nano-optoelectronics, etc.

Keywords: holography; metasurface; nanoprinting; orientation degeneracy; polychromatic.

1 Introduction

With the ultrathin thickness and subwavelength dimensions, nanostructured metasurfaces have unparalleled capabilities of realizing arbitrary manipulations of the electromagnetic fields. Polarization [1–6], amplitude [7–11], phase [12–16], and frequency [17–20] can be meticulously controlled by changing the dimensions and orientations of the nanostructures. With the characteristics of ultracompactness, high compatibility, low loss, and high resolution, metasurfaces have pointed out a new direction to design and fabricate novel electromagnetic devices, such as metalenses [21–26], vortex beam generators [27–31], holograms [32–37], nanoprints [38–40], etc. Thus, metasurfaces inject new vitality to promising applications in the fields of beam shaping [41–44], anti-counterfeiting [45–47], and optical storage [48]. In recent years, polarization multiplexing has drawn lots of attention [49–51]. However, currently proposed approaches for polarization multiplexing are generally conducted under two orthogonal polarization states, e.g., LP light along x/y axes and circularly polarized (CP) light with opposite handedness, due to that two orthogonally polarized light have no interference with each other. And orthogonal polarization multiplexing for metasurfaces is generally realized by varying the dimensions of nanostructures

*Corresponding author: Guoxing Zheng, Electronic Information School, Wuhan University, Wuhan, China; Peng Cheng Laboratory, Shenzhen, China; and NOEIC, State Key Laboratory of Optical Communication Technologies and Networks, Wuhan Research Institute of Posts & Telecommunications, Wuhan, China, E-mail: gxzheng@whu.edu.cn. https://orcid.org/0000-0002-3226-4735
Renyuan Ren, Zile Li, Liangui Deng, Xin Shan and Qi Dai, Electronic Information School, Wuhan University, Wuhan, China
Zhiqiang Guan, School of Physics and Technology, Wuhan University, Wuhan, China. https://orcid.org/0000-0001-5087-6439
Shaohua Yu, Peng Cheng Laboratory, Shenzhen, China; and NOEIC, State Key Laboratory of Optical Communication Technologies and Networks, Wuhan Research Institute of Posts & Telecommunications, Wuhan, China

[26, 52], which sharply increases the design and fabrication difficulty. Hence, the application scenarios would be limited. Since multi-channel information encoding plays a key role in many applications such as AR/VR displays and high-density optical storage, developing new approach for polarization multiplexing is important in advanced metasurface research.

Recently, benefitting from the orientation degeneracy derived from the Malus' law, one metasurface with single-size design can achieve multi-image encoding [53–55]. Not only the design, but also the fabrication is dramatically simplified, while the information density is significantly improved. In this work, we combine the supercell design with the orientation degeneracy of the Malus' law to demonstrate a non-orthogonal polarization multiplexed metasurface with tri-channel polychromatic image displays. We meticulously design and arrange the orientation angles of the nanostructures with only two different sizes to modulate the proportions of the red and green components. With the help of the orientation degeneracy, the intensities and phases of the red and green components can be independently modulated under three non-orthogonal polarization states incidence. As a result, one continuous-brightness polychromatic nanoprinting image, one binary-brightness polychromatic nanoprinting image, and one continuous-brightness polychromatic holographic image are simultaneously encoded into a single metasurface. More interestingly, in another design strategy with the same metasurface, up to six independent image-encodings and encryptions can be achieved, which not only increases the channel numbers of metasurfaces, but also provides a safe way for information encoding. With the advantages of colour mixing, high information density, high resolution, and high security, the proposed non-orthogonal polarization multiplexed metasurfaces can provide a simple way for information multiplexing, and may have promising applications in the fields of colour image encoding, anti-counterfeiting, optical storage, information encryption, etc.

2 Results and discussion

2.1 Working principles of the non-orthogonal polarization multiplexed metasurface for tri-channel polychromatic image displays

As shown in Figure 1, the proposed non-orthogonal polarization multiplexed metasurface is capable of recording three independent polychromatic images, including one continuous-brightness polychromatic nanoprinting image, one binary-brightness polychromatic nanoprinting image, and one continuous-brightness polychromatic holographic image. Here, the "continuous-brightness" means that the grayscales of meta-image's red and green components can be continuously modulated, i.e., each one ranges from 0 to 255 to form an 8-bit picture. To achieve the simultaneous recording of the aforementioned images, we employ the supercell design strategy with two dimension-types of nanobricks acting as half-wave plates (HWPs) working in the red and green spectra, respectively. Since the refection spectra of the two types of nanobricks have little crosstalk, red and green components of the reflected light can be arbitrarily and independently controlled without interfering with each other (see Methods for details about the reflectivities of the nanobricks). Hence, by elaborately arranging the numbers and orientation angles of the nanobricks responsible for red and green components, a colour mixing scheme with a gradient moving from red through yellow and finally to green can be achieved in near-field channel 1, and four colours can be mixed in near-field channel 2, which are red, green, yellow, and black. For far-field holographic image in channel 3, the phases of red and green components are individually optimized and the two holographic images are mixed to form the target polychromatic image. The proposed supercell structure contains four sub-cells, three of them are designed to reflect green light and one reflects red light, since the nanobricks responsible for reflecting green light has a relatively low cross-polarization efficiency. The polarization states and phases of red and green components can be manipulated by configuring the orientation angles of the sub-cells within a supercell.

In the near field, nanoprinting patterns require independent intensity modulation for the red and green components for colour mixing. Here, both the red and green components of the near-field images apply the same design approach as follows. When the incident light with the intensity of I_0 goes through a bulky polarizer, an anisotropic nanostructure acting as a nano-HWP, and a bulky analyser sequentially, governed by Malus' law and the polarization modulation property the HWP possesses, the intensity of the output light can be expressed as

$$I_R = I_0 \cos^2 (2\theta - \alpha_1 - \alpha_2), \tag{1}$$

where θ is the in-plane orientation angle of the nanobrick, and α_1 and α_2 are the polarization directions of the bulky polarizer and analyser, respectively. When the polarization directions of the polarizer and analyser are fixed at $\alpha_1 = \pi/4$

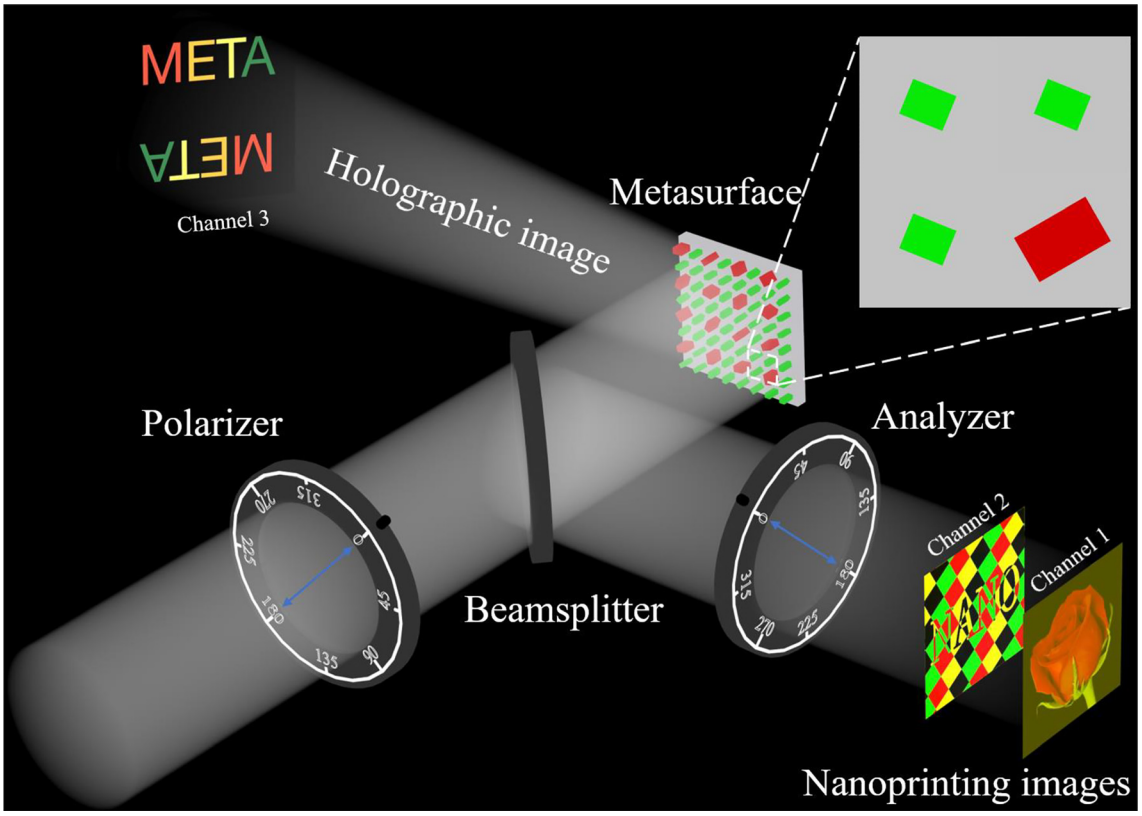

Figure 1: Diagram of the non-orthogonal polarization multiplexed metasurface for tri-channel polychromatic image displays. One continuous-brightness polychromatic nanoprinting image, one binary-brightness polychromatic nanoprinting image, and one continuous-brightness polychromatic holographic image are encoded into a single metasurface. The near-field images appear right at the metasurface plane and can be decoded with the help of a bulky polarizer and an analyser, with two different polarization combinations. The far-field holographic image can be reconstructed under laser incidence at two specific wavelengths without polarization control. Here, supercell design strategy is employed to independently manipulate the red and green lights for colour mixing.

and $\alpha_2 = 3\pi/4$, the intensity of the output light can be simplified to

$$I_{r1} = I_0 \cos^2 2\theta, \tag{2}$$

Here, I_{r1} represents the intensity modulation property in channel 1. Then, we keep the polarization directions of the polarizer and analyser unchanged, while rotating the metasurface by $\pi/8$, i.e., we rotate both the polarizer and analyser to the same direction by $\pi/8$. For every single nanostructure of the metasurface, it can be regarded as a $\pi/8$ reduction of the orientation angle. Hence, the intensity of the output light can be written as

$$I_{r2} = I_0 \cos^2\left(2\theta - \frac{\pi}{4}\right), \tag{3}$$

where I_{r2} represents the intensity modulation property in channel 2. The working principle of the dual-channel near-field intensity modulation is illustrated in Figure 2(a). For every sub-pixel within a pixel, it is obvious that the black dotted line representing a specific intensity has four black cross-marked points of intersection, #1, #2, #3, and #4 with I_{r1}, which indicates that to achieve a specific intensity modulation of the sub-pixel in channel 1, there are four orientation angle candidates of the nanobrick. For the same sub-pixel in channel 2, the intensity value can be chosen to be higher or lower than 0.5. Specifically, to realize a higher value modulation, there are two orientation choices, #1 and #3, while the rest of the two orientation angles #2 and #4 can be used to achieve a lower value modulation. Via this approach, the continuous modulation and binary modulation of both the red and green components are realized in channels 1 and 2, respectively. It should be noted that the binary intensity value of channel 2 is related to the intensity value of channel 1, which would affect the brightness and colour mixing. However, the calculated results shown in Section 1 of Supplementary Material indicate that the average deviations have little influence on colours.

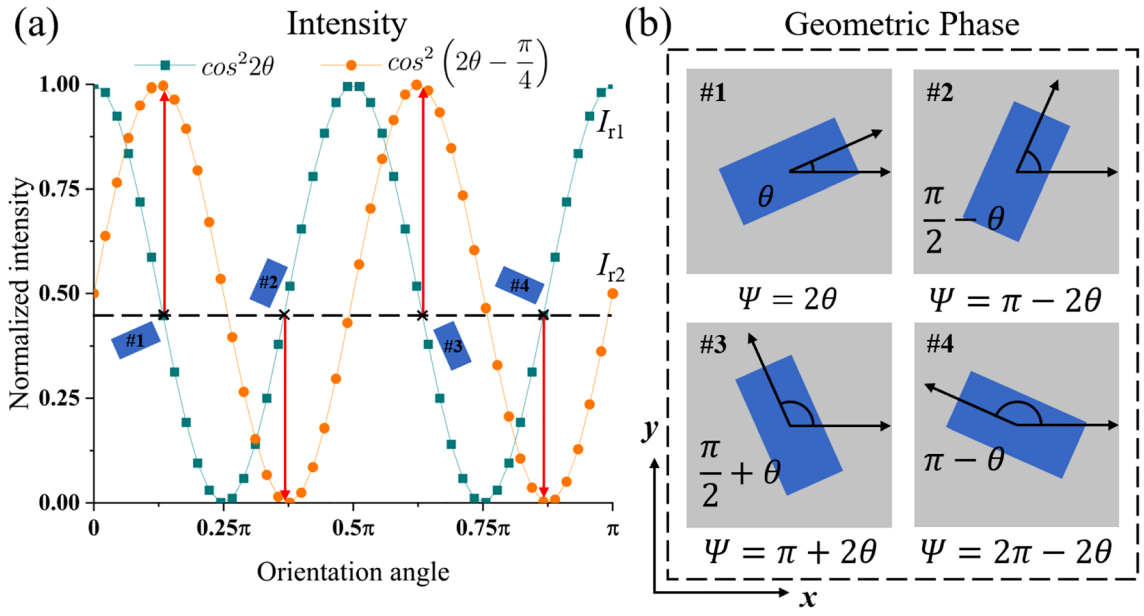

Figure 2: Working principles of the non-orthogonal polarization multiplexed metasurface for simultaneous dual-intensity and phase modulations.
(a) Near-field intensity modulation scheme of the metasurface. When the bulky polarizer and analyser are rotated to two different polarization combinations, i.e., ($\pi/4$, $3\pi/4$) and ($3\pi/8$, $7\pi/8$), the intensity of the incident light in channels 1 and 2 can be modulated according to two different modulation functions I_{r1} and I_{r2}. For a pixel with the specific intensity in channel 1, there are four orientation candidates for each nanobrick. For the same pixel with the binary value in channel 2, two of four are qualified, depending on whether the value is above 0.5 or below 0.5. (b) Phase modulation scheme of the metasurface. The geometric phase is equal to twice the orientation angle. It should be noted that only two of the four candidates are available since the intensity modulation should meet the requirements in channels 1 and 2.

Moreover, every nanobrick can be allocated two orientation angles to realize the two nanoprinting images encoding, which leaves a degree of freedom and makes it possible to encode another polychromatic holographic image, enabled with geometric phase.

In the far field, benefitting from the design freedom of the orientation degeneracy mentioned above, each nanobrick has two orientation angle options to achieve the desired intensities in the defined orientation interval $[0, \pi]$, which indicates that a two-step geometric phase encoding can be achieved and a phase-only holographic image can be generated under CP light illumination. When the CP light is incident on the nanobrick, the cross-polarized (cro-pol) part of the reflected light is added with an additional geometric phase, which is exactly twice the orientation angle of the nanobrick, as shown in Figure 2(b), while the co-polarized (co-pol) part of the reflected light remains unchanged. Therefore, the Simulated Annealing (SA) algorithm can be employed to optimize the phases of the red and green components. It is worth noting that the two-step phase encoding method brings about a phenomenon that the holographic image should be centrosymmetric, which is a double-edged sword. The range of the picture available is limited to a half reflection space, while the experimental setup of the reconstruction is simplified, because the polarization state of the incident light is no longer required (more details about two-step phase holography and experimental setup can be found in Section 2, Supplementary Material).

By applying the scheme mentioned above, intensity, phase, and spectrum of the reflected light can be simultaneously manipulated. Hence, one metasurface is able to record three independent images under three non-orthogonal polarization light incidence, two near-field polychromatic nanoprinting images with continuous-brightness and binary-brightness can be realized, and a far-field continuous-brightness polychromatic holographic image can be reconstructed in the Fraunhofer diffraction zone.

2.2 Design and experimental demonstration of the non-orthogonal polarization multiplexed metasurface

Based on the simultaneous intensity, phase, and spectrum manipulation of light, we design a non-orthogonal polarization multiplexed metasurface for achieving

polychromatic dual-nanoprinting and holography. The metasurface is based on silicon-on-sapphire (SOS) material which consists of silicon nanobricks sitting on a sapphire substrate, and the unit-cell design is conducted under a commercial software (CST Microwave studio). Though the Al_2O_3 substrate of SOS material possesses the characteristic of anisotropy, it does not influence the polarization property of the reflected light, since the unusual high-reflection is caused by the magnetic resonance of dielectric nanobricks. Therefore, the light hardly passes through the anisotropic substrate (detailed discussion about the influence of anisotropic property of the substrate can be found in Section 3, Supplementary Material). Here, two types of nanobricks (named as red nanobrick and green nanobrick) are designed to have the identical sub-cell size 300 nm and height 230 nm. Each supercell contains four sub-cells, including one red nanobrick and three green nanobricks. The lengths and widths of the red and green nanobricks are different (see Methods for details about the nanobricks design). Within the supercell, three green nanobricks have the same orientation angle, while between different supercells, orientation angles of nanobricks are determined by the recorded images, according to Equations (2) and (3). In our design, the multiplexing metasurface consists of 500 × 500 pixels (300 × 300 μm^2). In the near field, we chose a rose picture as the target image for polychromatic nanoprinting. The reason that we chose a rose picture lies that it mainly consists of red and green colours, and the brightness of each colour component is continuously modulated. For another nanoprinting picture, we design an image consisting of letters "NANO" in the centre, and colour blocks in the background. Here, to make the letters stand out from the background, we define two pairs of contrasting colours, which are red corresponding to green and yellow corresponding to black. In the far field, we generate an image with letters "META", and the colours of four letters differ. Hence, the monochromic brightness of each letter is different to obtain different mixed colours. We calculate the orientation angle distribution of the red and green components separately based on the near-field images. Then, we employ the SA algorithm to choose between the two options pixel-by-pixel to optimize the phase profile to reconstruct the target holographic image. The whole design flowchart is illustrated in Figure 3.

The standard electron-beam lithography (EBL) is employed to fabricate the aforementioned metasurface sample (see more fabrication details in Methods) and Figure 4(a) shows the scanning electron microscope (SEM) image in partial view. For near-field nanoprinting images, a commercial optical microscope (Motic BA310MET-T) is applied, as shown in Figure 4(b). Firstly, a halogen lamp is used to generate the wide-band light, the light passes through a bulky polarizer, which changes the incident light's polarization state to LP. Secondly, the LP light illuminates the metasurface sample, which reflects the light and modulates the spectrum and polarization direction of

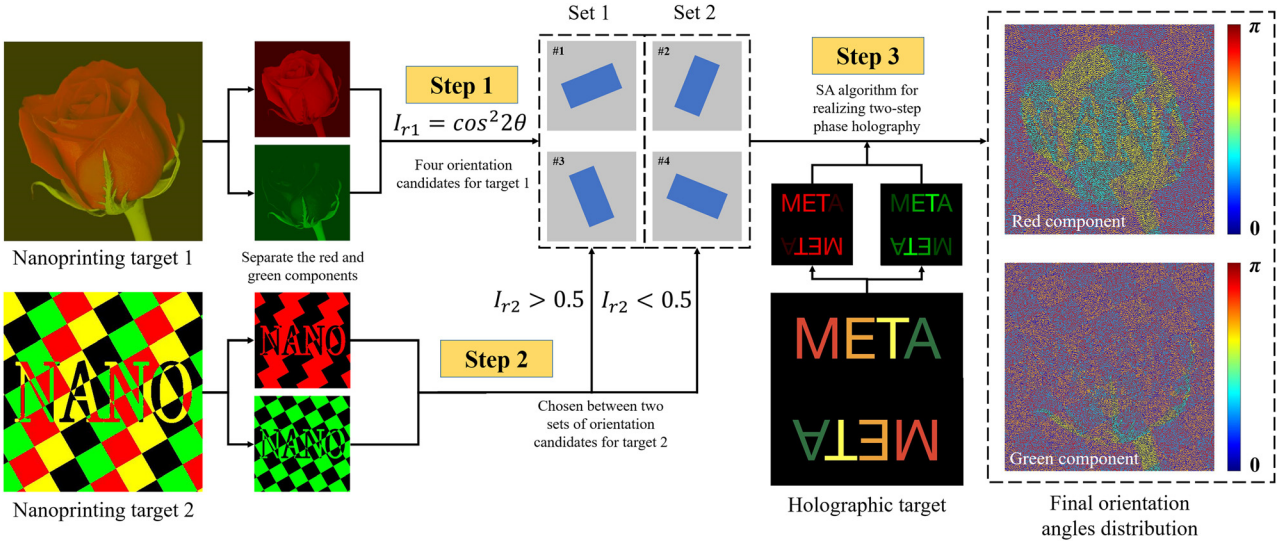

Figure 3: Design flowchart of the non-orthogonal polarization multiplexed metasurface.
We separate the red and green components of each image and the two components follow the same design procedure. Firstly, four orientation candidates can be deduced due to the modulation function I_{r1} based on the nanoprinting target 1. Secondly, according to the intensity of the nanoprinting target 2, four orientation candidates are divided into two sets and one of them is picked. Finally, we employ the SA algorithm to realize a two-step phase holography. The red and green components can be remixed to achieve colour mixing.

the LP light pixel-by-pixel. After that, an analyser is employed to modulate the intensity of the reflected light. Finally, the output LP light possesses spatially varied intensity and spectrum, a commercial camera (Moticam X) is used to capture the light after being magnified by a 50× objective. Figure 4(c) and (d) exhibits the experimental results of the nanoprinting images in channels 1 and 2, respectively. And the polarization directions of the polarizer and analyser for each channel are indicated on the top by red and blue arrows, respectively. For channel 1, the mixing of continuous-brightness red and green components forms the polychromatic meta-image. And for channel 2, each sub-cell has only two choices: bright (red/green) or dark (black). Therefore, there are four colours in channel 2: red, green, black, and yellow (the mixing of red and green). All experimentally captured images can be seen clearly and the colours do not deviate much from the target images.

As for holographic image, we employ a supercontinuum laser source (YSL SC-pro) to generate a laser beam with the wavelengths of 633 nm for red and 525 nm for green. The reason why we do not choose the wavelengths with the highest theoretical cro-pol efficiency is to lower down the crosstalk between two reflected spectra and reduce the unwanted zero-order light. As mentioned above, due to the fact that two-step phase encoding results in centrosymmetric image, the polarization controlling of the laser beam in reconstruction process is unnecessary, which significantly simplifies the optical setup, as exhibited in Figure 4(e). Therefore, the laser beam generated from laser source is directly and normally incident on the metasurface sample after passing through an iris. The metasurface reflects the light to a white screen, and the holographic image is reconstructed and can be observed on the white screen through bare eyes. After that, we utilize a commercial camera (Nikon D5100) to capture the reconstructed holographic image. Figure 4(f) shows the experimentally captured picture of the reconstructed holographic image in channel 3. The centrosymmetric image of the letters “META” in four different colours can be observed clearly. Here, the optical efficiencies (defined as the ratio of the power of the

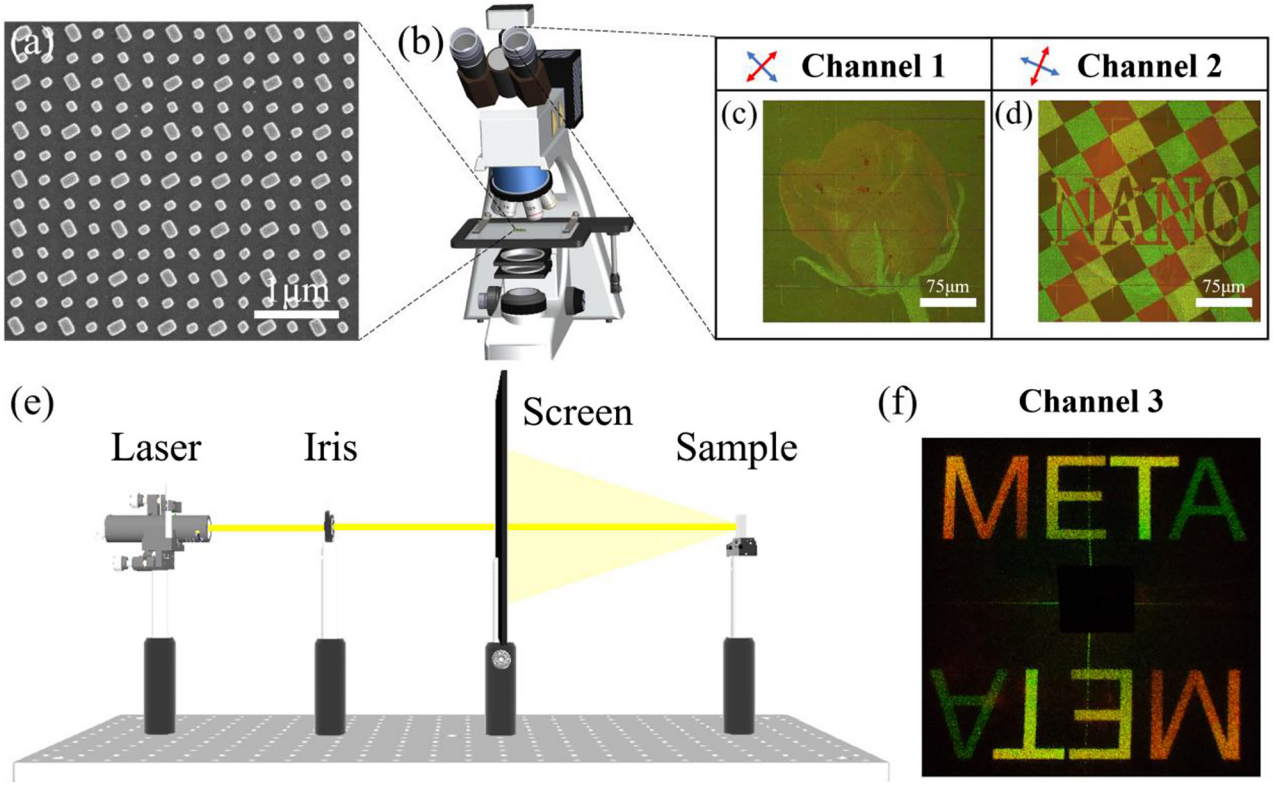

Figure 4: Experimental setups and results of the non-orthogonal polarization multiplexed metasurface.
(a) Partial view of the SEM image of the fabricated metasurface. The scale bar is 1 μm. (b) Experimental setup for capturing nanoprinting images. (c) and (d) Experimentally captured polychromatic nanoprinting images under halogen lamp illumination in channels 1 and 2, respectively. The scale bars are 75 μm. Red and blue arrows on the top indicate the polarization directions of the bulky polarizer and analyser, respectively. (e) Optical path setup for holography. (f) Experimentally obtained polychromatic holographic image under laser beam illumination.

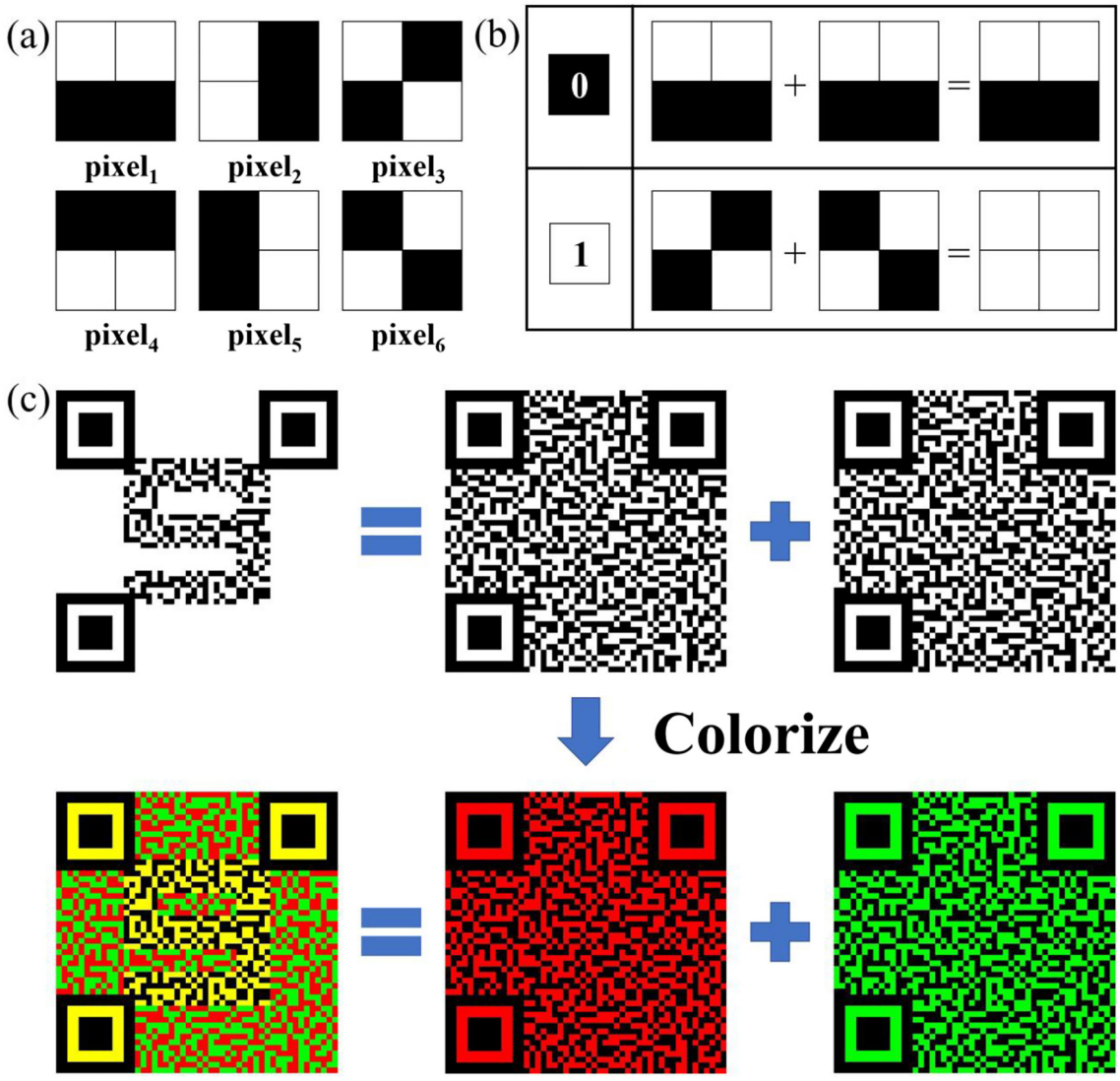

Figure 5: Schematic diagram of the binary encryption procedure based on VC algorithm.
(a) Six types of 2 × 2 expanded pixels, which can be used in expansion and superposition. (b) Instance of the "0" and "1" pixel's expansion and superposition. (c) Procedure of the encryption. The encrypted image is expanded by randomly picking 2 × 2 pixels and transformed into two binary images according to the superposition of the pixels. The two binary images are faked as QR codes by adding positioning blocks and encoded into two wavelength channels. The decryption can be conducted under white light illumination.

generated images to the power of the incident light) at two working wavelengths (633 and 525 nm) are measured, which are 7.32 and 18.90% for red and green components, respectively (details about measurement configuration can be found in Section 4, Supplementary Material). What is noteworthy is that according to the diffraction theory, the size of the holographic image is proportional to the wavelength. Thus, we conduct a pre-process to adjust the sizes of the red and green components. And by this way, the red and green components of the reconstructed holographic image can match well with each other. In addition, the broadband functionality and efficiency of the sample have been explored (more details about broadband experiments, broadband efficiency measurements, and the efficiency analysis are included in Section 4, Supplementary Material).

2.3 Six-image encodings and encryptions with the proposed metasurface

To further investigate the independent record of the red and green components of the proposed metasurface, another metasurface sample with six independent images is

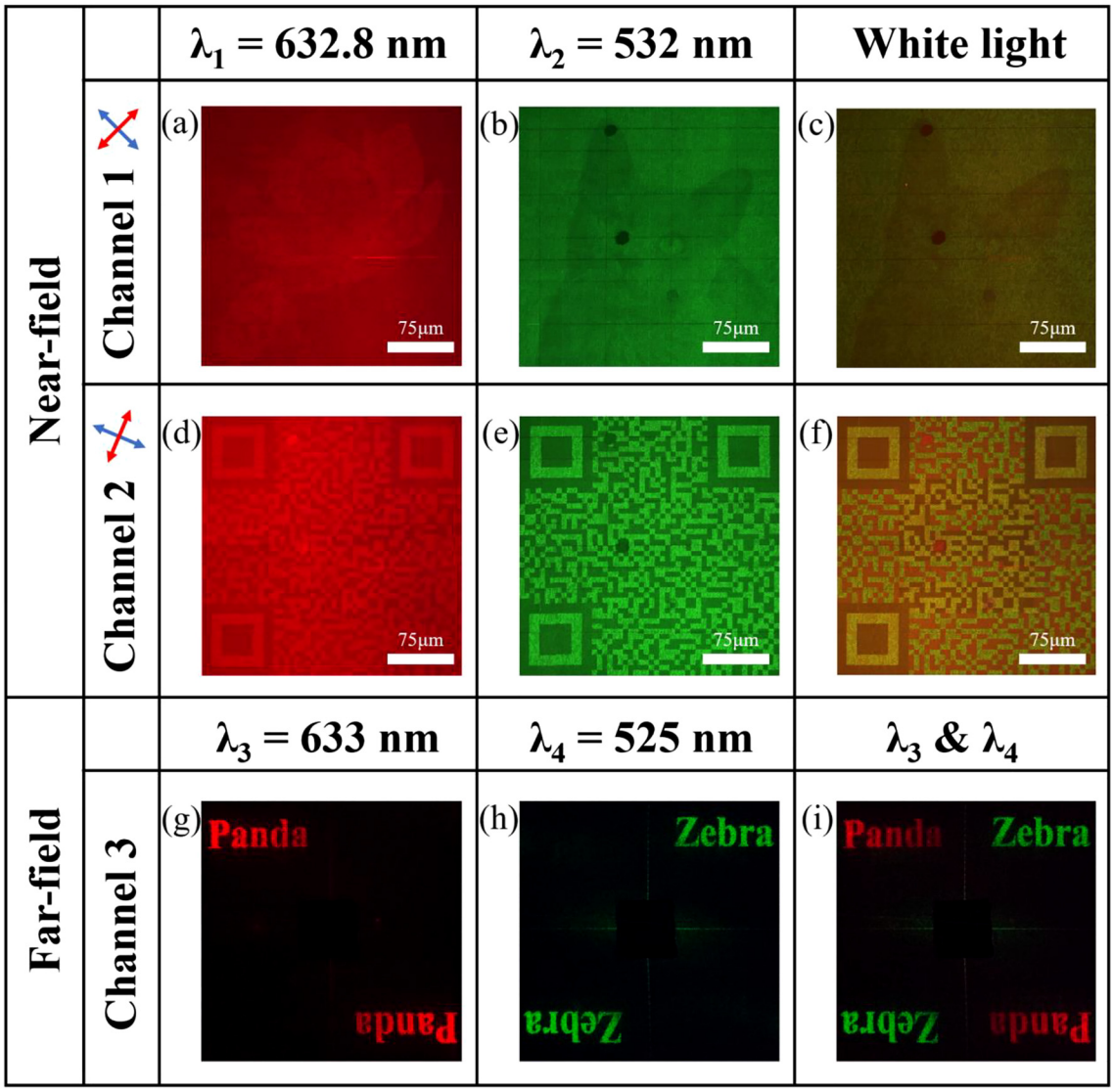

Figure 6: Experimentally obtained results of the six independent images and the encrypted information.
(a)–(f) The captured images in channels 1 and 2 under 632.8, 532 nm, and white light illumination, respectively. The single wavelength illumination and white light illumination are realized by inserting optical filters and a halogen lamp, respectively. Scale bars of 75 μm are marked on all images. The red and green arrows indicate the polarization direction of polarizer and analyser, respectively. (g)–(i) Experimentally captured holographic images under 633, 525 nm and the two wavelengths together, respectively. The illumination is realized by a super-continuum laser source.

designed and fabricated, which includes two near-field grayscale images, two near-field binary images, and two holographic images. In addition, the two near-field binary images are designed as fake QR codes to realize encryption based on visual cryptography (VC) algorithm [56]. In the classical VC algorithm, every pixel of the encrypted image can be expanded and regarded as the superposition of two 2×2 pixels, and an example with six types of pixels is illustrated in Figure 5(a). Pixel with the value of "0" and "1" can be transformed into two 2×2 pixels picked from these six types, as shown in Figure 5(b). Here, adding pixel_1 and pixel_4, pixel_2 and pixel_5, pixel_3 and pixel_6 can form "1", while adding pixels and themselves can realize "0". Figure 5(c) exhibits the procedure of the encryption. Firstly, "0" pixels of the encrypted image are randomly expanded to six types of 2×2 pixels and the encrypted image is transformed into two images based on the scheme aforementioned. Then, three positioning blocks are added to the images to form the fake QR codes. Finally, the two fake QR codes are encoded into two different wavelengths. The

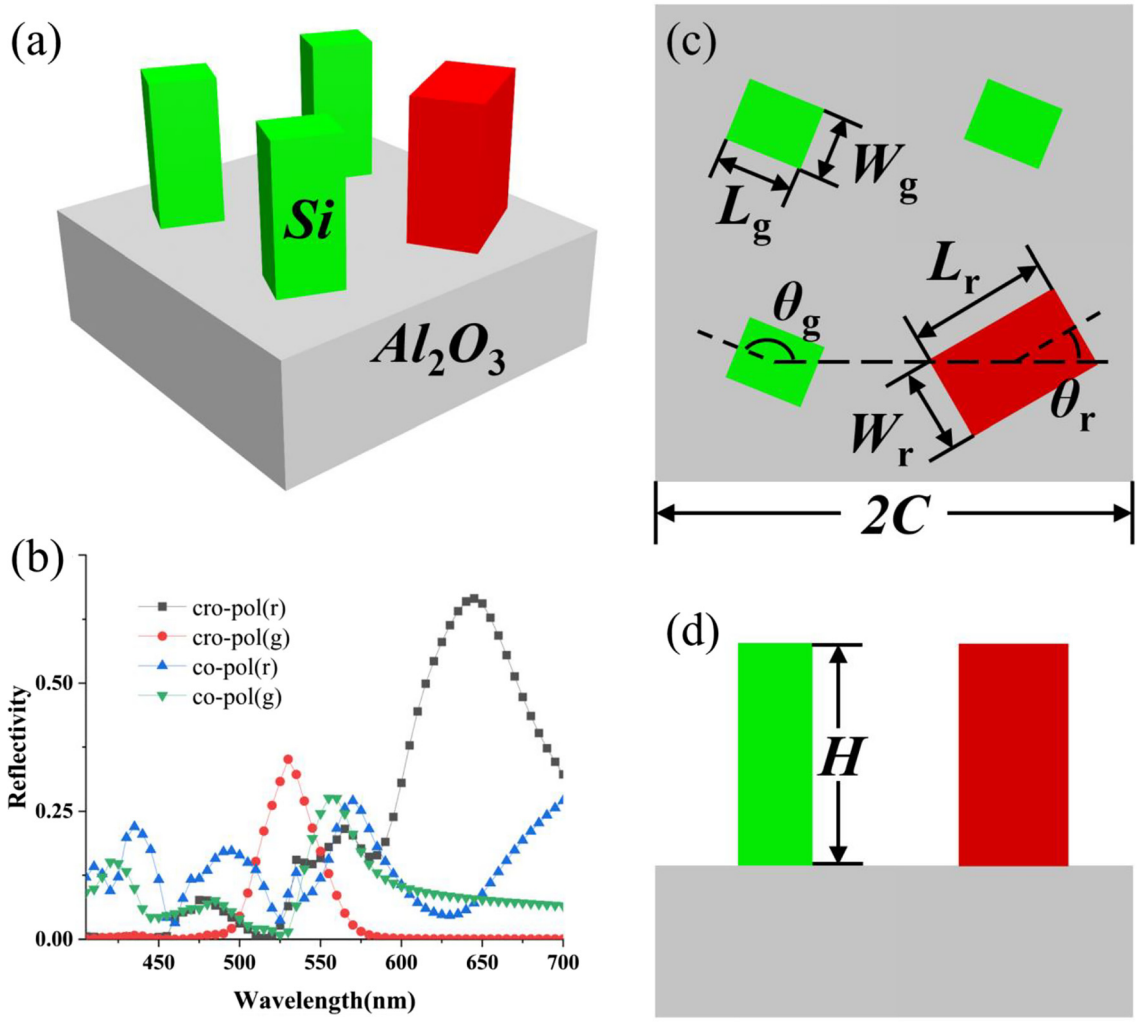

Figure 7: Illustration of a unit cell of the metasurface and the simulation results.
(a) Schematic diagram of the supercell nanostructure, which includes Si nanobricks sitting on an Al_2O_3 substrate. (b) Reflectivities of the output cro-pol and co-pol parts under CP light illumination, "*r*" and "*g*" in the parentheses indicate the red and green nanobricks, respectively. (c) Top view of the supercell nanostructure, which consists of four sub-cells with the same sub-cell size of 300 nm. Red nanobricks have the dimensions of 180 nm in length (L_r) and 110 nm in width (W_r). Green nanobricks have the dimensions of 100 nm in length (L_g) and 80 nm in width (W_g). (d) Side view of the supercell nanostructure. The Silicon nanobricks layer has a fixed height of 230 nm.

superposition of the two wavelengths indicates that the decryption can be realized under white light illumination.

The experiment is conducted to verify the six-image encoding and encryption property of the proposed metasurface. Figure 6(a)–(f) illustrates the near-field nanoprinting images in channels 1 and 2 under 632.8, 532 nm, and white light illumination, respectively. The narrow band illumination is realized by inserting optical filters with the bandwidth of 10 nm. Specifically, a lotus image, a cat image, and two fake QR codes can be observed in the near field. It is obvious that the four near-field nanoprinting images have negligible crosstalk with each other. Under the halogen lamp illumination, the encrypted image with the number "9" can be revealed. Figure 6(g)–(i) shows the holographic images in channel 3 under laser beam incidence with the wavelengths of 633, 525 nm, and both together. All experimental results show that the six meta-images have negligible crosstalk, and by subtly combining the images with encryption algorithms, information can be securely concealed and delivered. Thus, the proposed metasurface has the property of completely independent encoding six images and the new function of information encryption.

3 Conclusions

In summary, we present a non-orthogonal polarization multiplexed metasurface for tri-channel near- and far-field polychromatic image displays, merely with a single-layer design approach. Our research shows that, even under non-orthogonal polarization light illumination and limi ted degrees of freedom of nanostructured metasurfaces, expanding the channel numbers and colour manipulation still can be realized with a minimalist design strategy: only two types of nanostructures are required to form the metasurface, which can significantly reduce the difficulties of both the design and fabrication. In another design strategy with the same metasurface, we show that up to six independent images, including two near-field grayscale images, two near-field binary images, and two holographic images, can be encoded into a single metasurface. Assisted by the VC algorithm, the aforementioned metasurface is endowed with a new function of information encryption. Therefore, with the advantages of ultracompactness, high-capacity, high-security, and multifunctionality, our proposed metasurfaces can be employed to achieve information multiplexing and encryption, and have potential in the fields of ultracompact and multi-channel image displays, optical anti-counterfeiting, optical storage, etc.

4 Methods

4.1 Unit cell design

Figure 7(a) illustrates a unit cell of the metasurface, which is composed of a Si nanobrick layer and an Al_2O_3 substrate layer. Figure 7(b) shows the cro-pol and co-pol parts of reflectivities of the red and green nanobricks with the chosen dimensions under CP light illumination. These two types of nanostructures are simulated separately as the unit cell. It is obvious that the peak wavelengths of the reflected cro-pol light are around 645 and 530 nm, and the reflectivities are above 66 and 35% at the two wavelengths for red and green nanobricks, respectively. Figure 7(c) and (d) exhibits the dimensions we optimize for red and green nanobricks. To reduce the coupling effect between the two types of nanobricks and decrease the difficulty of designing the supercell, both of the red and green nanobricks are designed to have the identical sub-cell size C = 300 nm, hence, the cell size of the supercell is $2C$ = 600 nm. Height of the nanobricks layer is fixed at H = 230 nm. Lengths and widths of the red and green nanobricks are labelled with subscripts "r" and "g", respectively. Here, in order to minimize the crosstalk between the reflected spectrums of the red and green nanobricks, we choose L_r = 180 nm, W_r = 110 nm, L_g = 100 nm, and W_g = 80 nm. θ_r and θ_g indicate the in-plane orientation angles of red and green nanobricks, respectively.

4.2 Sample fabrication

A standard EBL process was employed to fabricate the sample on an SOS wafer. Firstly, acetone, alcohol, and deionized water were successively used to ultrasonically clean the sample. Secondly, the conducting adhesive was evenly applied on the SOS wafer. A standard electron beam process was employed to pattern a polymethacrylate (PMMA) mask on the sample. Before developing the sample, the conducting adhesive was washed away by the water. Then, as an etch mask, a 30 nm Cr film was deposited by a thermal evaporator, followed by a lift-off process in hot acetone of 75 °C. After that, the reactive ion etching (RIE) method was employed to remove the Cr-free part. Finally, the sample was soaked in the Cr etchant for one night. Thus, the fabrication of the sample was accomplished.

Author contributions: R. Ren and Z. Li contributed equally. All the authors have accepted responsibility for the entire content of this submitted manuscript and approved submission.

Research funding: This work was supported by the National Natural Science Foundation of China (Nos. 91950110, 11774273 and 11904267), the China Postdoctoral Science Foundation (2019M652688), and the Natural Science Foundation of Jiangsu Province (BK20190211).

Conflict of interest statement: The authors declare no conflicts of interest regarding this article.

References

[1] S. Wang, Z. Deng, Y. Wang, et al., "Arbitrary polarization conversion dichroism metasurfaces for all-in-one full Poincaré sphere polarizers," *Light Sci. Appl.*, vol. 10, p. 24, 2021.

[2] D. Wang, F. Liu, T. Liu, et al., "Efficient generation of complex vectorial optical fields with metasurfaces," *Light Sci. Appl.*, vol. 10, p. 67, 2021.

[3] Q. Song, S. Khadir, S. Vézian, et al., "Bandwidth-unlimited polarization-maintaining metasurfaces," *Sci. Adv.*, vol. 7, p. eabe1112, 2021.

[4] K. Tanaka, D. Arslan, S. Fasold, et al., "Chiral bilayer all-dielectric metasurfaces," *ACS Nano*, vol. 14, pp. 15926–15935, 2020.

[5] L. Wu, H. Ma, R. Wu, et al., "Transmission-reflection controls and polarization controls of electromagnetic holograms by a reconfigurable anisotropic digital coding metasurface," *Adv. Opt. Mater.*, vol. 8, p. 2001065, 2020.

[6] Z. Li, S. Yu, and G. Zheng, "Advances in exploiting the degrees of freedom in nanostructured metasurface design: from 1 to 3 to more," *Nanophotonics*, vol. 9, pp. 3699–3731, 2020.

[7] Z. L. Deng, M. Jin, X. Ye, et al., "Full-color complex-amplitude vectorial holograms based on multi-freedom metasurfaces," *Adv. Funct. Mater.*, vol. 30, p. 1910610, 2020.

[8] F. Yue, C. Zhang, X. F. Zang, et al., "High-resolution grayscale image hidden in a laser beam," *Light Sci. Appl.*, vol. 7, p. 17129, 2018.

[9] R. Fu, L. Deng, Z. Guan, et al., "Zero-order-free meta-holograms in a broadband visible range," *Photonics Res.*, vol. 8, pp. 723–728, 2020.
[10] G. Zheng, R. Fu, L. Deng, and Z. Li, "On-axis three-dimensional meta-holography enabled with continuous-amplitude modulation of light," *Opt. Express*, vol. 29, pp. 6147–6157, 2021.
[11] Q. Dai, L. Deng, J. Deng, et al., "Ultracompact, high-resolution and continuous grayscale image display based on resonant dielectric metasurfaces," *Opt. Express*, vol. 27, pp. 27927–27935, 2019.
[12] G. Zheng, H. Mühlenbernd, M. Kenney, G. Li, T. Zentgraf, and S. Zhang, "Metasurface holograms reaching 80% efficiency," *Nat. Nanotechnol.*, vol. 10, pp. 308–312, 2015.
[13] Q. Cheng, J. Wang, L. Ma, et al., "Achromatic terahertz Airy beam generation with dielectric metasurfaces," *Nanophotonics*, vol. 10, pp. 1123–1131, 2020.
[14] R. Kaissner, J. Li, W. Lu, et al., "Electrochemically controlled metasurfaces with high-contrast switching at visible frequencies," *Sci. Adv.*, vol. 7, p. eabd9450, 2021.
[15] Z. Li, Q. Dai, M. Q. Mehmood, et al., "Full-space cloud of random points with a scrambling metasurface," *Light Sci. Appl.*, vol. 7, p. 63, 2018.
[16] Z. Li, I. Kim, L. Zhang, et al., "Dielectric meta-holograms enabled with dual magnetic resonances in visible light," *ACS Nano*, vol. 11, pp. 9382–9389, 2017.
[17] C. Schlickriede, N. Waterman, B. Reineke, et al., "Imaging through nonlinear metalens using second harmonic generation," *Adv. Mater.*, vol. 30, p. 1703843, 2018.
[18] F. Spreyer, R. Zhao, L. Huang, and T. Zentgraf, "Second harmonic imaging of plasmonic Pancharatnam-Berry phase metasurfaces coupled to monolayers of WS2," *Nanophotonics*, vol. 9, pp. 351–360, 2020.
[19] B. Reineke, B. Sain, R. Zhao, et al., "Silicon metasurfaces for third harmonic geometric phase manipulation and multiplexed holography," *Nano Lett.*, vol. 19, pp. 6585–6591, 2019.
[20] G. Li, S. Chen, N. Pholchai, et al., "Continuous control of the nonlinearity phase for harmonic generations," *Nat. Mater.*, vol. 14, pp. 607–612, 2015.
[21] K. Dou, X. Xie, M. Pu, et al., "Off-axis multi-wavelength dispersion controlling metalens for multi-color imaging," *Opto-Electron. Adv.*, vol. 3, p. 190005, 2020.
[22] J. Li, Y. Wang, C. Chen, et al., "From lingering to rift: metasurface decoupling for near- and far-field functionalization," *Adv. Mater.*, vol. 33, p. 2007507, 2021.
[23] S. Wang, P. C. Wu, V. C. Su, et al., "A broadband achromatic metalens in the visible," *Nat. Nanotechnol.*, vol. 13, pp. 227–232, 2018.
[24] W. T. Chen, A. Y. Zhu, V. Sanjeev, et al., "A broadband achromatic metalens for focusing and imaging in the visible," *Nat. Nanotechnol.*, vol. 13, pp. 220–226, 2018.
[25] S. Colburn, A. Zhan, and A. Majumdar, "Varifocal zoom imaging with large area focal length adjustable metalenses," *Optica*, vol. 5, pp. 825–831, 2018.
[26] R. Fu, Z. Li, G. Zheng, et al., "Reconfigurable step-zoom metalens without optical and mechanical compensations," *Opt. Express*, vol. 27, pp. 12221–12230, 2019.
[27] Y. Guo, M. Pu, Z. Zhao, et al., "Merging geometric phase and plasmon retardation phase in continuously shaped metasurfaces for arbitrary orbital angular momentum generation," *ACS Photonics*, vol. 3, pp. 2022–2029, 2016.
[28] P. Yu, J. Li, X. Li, et al., "Generation of switchable singular beams with dynamic metasurfaces," *ACS Nano*, vol. 13, pp. 7100–7106, 2019.
[29] H. M. Leung, W. Gao, R. Zhang, et al., "Exceptional point-based plasmonic metasurfaces for vortex beam generation," *Opt. Express*, vol. 28, pp. 503–510, 2020.
[30] J. Han, Y. Intaravanne, A. Ma, et al., "Optical metasurfaces for generation and superposition of optical ring vortex beams," *Laser Photonics Rev.*, vol. 14, p. 2000146, 2020.
[31] M. Pu, X. Li, X. Ma, et al., "Catenary optics for achromatic generation of perfect optical angular momentum," *Sci. Adv.*, vol. 1, p. e1500396, 2015.
[32] Y. Hu, L. Li, Y. Wang, et al., "Trichromatic and tripolarization-channel holography with noninterleaved dielectric metasurface," *Nano Lett.*, vol. 20, pp. 994–1002, 2020.
[33] Q. Jiang, G. Jin, and L. Cao, "When metasurface meets hologram: principle and advances," *Adv. Opt. Photonics*, vol. 11, pp. 518–576, 2019.
[34] Q. Dai, Z. Guan, S. Chang, et al., "A single-celled tri-functional metasurface enabled with triple manipulations of light," *Adv. Funct. Mater.*, vol. 30, p. 2003990, 2020.
[35] J. Li, S. Kamin, G. Zheng, F. Neubrech, S. Zhang, and N. Liu, "Addressable metasurfaces for dynamic holography and optical information encryption," *Sci. Adv.*, vol. 4, p. eaar6768, 2018.
[36] G. Zheng, N. Zhou, L. Deng, G. Li, J. Tao, and Z. Li, "Full-space metasurface holograms in the visible range," *Opt. Express*, vol. 29, pp. 2920–2930, 2021.
[37] C. Choi, S. Mun, J. Sung, K. Choi, S. Lee, and B. Lee, "Hybrid state engineering of phase-change metasurface for all-optical cryptography," *Adv. Funct. Mater.*, vol. 31, p. 2007210, 2021.
[38] J. Jang, H. Jeong, G. Hu, C. Qiu, K. Nam, and J. Rho, "Kerker-conditioned dynamic cryptographic nanoprints," *Adv. Opt. Mater.*, vol. 7, p. 1801070, 2019.
[39] Q. Dai, N. Zhou, L. Deng, J. Deng, Z. Li, and G. Zheng, "Dual-channel binary gray-image display enabled with Malus-assisted metasurfaces," *Phys. Rev. Appl.*, vol. 14, p. 034002, 2020.
[40] H. Liu, W. Dong, H. Wang, et al., "Rewritable color nanoprints in antimony trisulfide films," *Sci. Adv.*, vol. 6, p. eabb7171, 2020.
[41] Y. Yang, W. Wang, P. Moitra, I. I. Kravchenko, D. P. Briggs, and J. Valentine, "Dielectric meta-reflectarray for broadband linear polarization conversion and optical vortex generation," *Nano Lett.*, vol. 14, pp. 1394–1399, 2014.
[42] K. Huang, H. Liu, S. Restuccia, et al., "Spiniform phase-encoded metagratings entangling arbitrary rational-order orbital angular momentum," *Light Sci. Appl.*, vol. 7, p. 17156, 2018.
[43] Y. Fu, C. Shen, Y. Cao, et al., "Reversal of transmission and reflection based on acoustic metagratings with integer parity design," *Nat. Commun.*, vol. 10, p. 2326, 2019.
[44] S. Chen, W. Liu, Z. Li, H. Cheng, and J. Tian, "Metasurface-empowered optical multiplexing and multifunction," *Adv. Mater.*, vol. 32, p. 1805912, 2020.
[45] L. Jin, Z. Dong, S. Mei, et al., "Noninterleaved metasurface for $(2^6\text{-}1)$ spin- and wavelength-encoded holograms," *Nano Lett.*, vol. 18, pp. 8016–8024, 2018.
[46] R. Zhao, B. Sain, Q. Wei, et al., "Multichannel vectorial holographic display and encryption," *Light Sci. Appl.*, vol. 7, p. 95, 2018.

[47] H. C. Liu, B. Yang, Q. Guo, et al., "Single-pixel computational ghost imaging with helicity-dependent metasurface hologram," *Sci. Adv.*, vol. 3, p. e1701477, 2017.
[48] H. Jiang and B. Kaminska, "Scalable inkjet-based structural color printing by molding transparent gratings on multilayer nanostructured surfaces," *ACS Nano*, vol. 12, pp. 3112–3125, 2018.
[49] J. P. B. Mueller, N. A. Rubin, R. C. Devlin, B. Groever, and F. Capasso, "Metasurface polarization optics: independent phase control of arbitrary orthogonal states of polarization," *Phys. Rev. Lett.*, vol. 118, p. 113901, 2017.
[50] I. Kim, J. Jang, G. Kim, et al., "Pixelated bifunctional metasurface-driven dynamic vectorial holographic color prints for photonic security platform," *Nat. Commun.*, vol. 12, p. 3614, 2021.
[51] J. Deng, Z. Li, G. Zheng, et al., "Depth perception based 3D holograms enabled with polarization-independent metasurfaces," *Opt. Express*, vol. 26, pp. 11843–11849, 2018.
[52] A. Arbabi, Y. Horie, M. Bagheri, and A. Faraon, "Dielectric metasurfaces for complete control of phase and polarization with subwavelength spatial resolution and high transmission," *Nat. Nanotechnol.*, vol. 10, pp. 937–943, 2015.
[53] J. Deng, L. Deng, Z. Guan, et al., "Multiplexed anticounterfeiting meta-image displays with single-sized nanostructures," *Nano Lett.*, vol. 20, pp. 1830–1838, 2020.
[54] L. Deng, J. Deng, Z. Guan, et al., "Malus-metasurface-assisted polarization multiplexing," *Light Sci. Appl.*, vol. 9, p. 101, 2020.
[55] Z. Li, C. Chen, and Z. Guan, "Three-channel metasurfaces for simultaneous meta-holography and meta-nanoprinting: A single-cell design approach," *Laser Photonics Rev.*, vol. 14, p. 2000032, 2020.
[56] N. Yang, Q. Gao, and Y. Shi, "Visual-cryptographic image hiding with holographic optical elements," *Opt. Express*, vol. 26, pp. 31995–32006, 2018.

Supplementary Material: The online version of this article offers supplementary material (https://doi.org/10.1515/nanoph-2021-0259).